

## Article

# Corrosion Performance of Epoxy/Sulfur–Selenium Coating on Q235 Steel

Konglan Meng<sup>1,2</sup>, Wei Wei<sup>1,2,\*</sup> , Kunxia Wei<sup>1,2,\*</sup>, Igor V. Alexandrov<sup>2,3</sup>, Xulong An<sup>1,2</sup>, Dandan Wang<sup>1,2</sup> and Xiangkui Liu<sup>1,2</sup>

<sup>1</sup> School of Materials Science and Engineering, Changzhou University, Changzhou 213164, China; 19172026074@163.com (K.M.); axl@cczu.edu.cn (X.A.); ddwang@cczu.edu.cn (D.W.); xkliu93@126.com (X.L.)

<sup>2</sup> CNPC-CZU Innovation Alliance, Jiangsu Key Laboratory of Materials Surface Science and Technology, Advanced Functional Materials of Jiangsu Joint Laboratory for International Cooperation, Changzhou University, Changzhou 213164, China; igorvalexandrov@yandex.ru

<sup>3</sup> Department of Materials Science and Physics of Metals, Ufa University of Science and Technology, 450008 Ufa, Russia

\* Correspondence: benjamin.wwei@163.com (W.W.); kunxiawei@163.com (K.W.)

**Abstract:** Sulfur powder (99.99%) and selenium powder (99.99%) were mixed and heated to approximately 300 °C to obtain an S-Se alloy. It has good flowability at 130 °C and can be applied to Q235 steel to obtain a S-Se coating. Epoxy was used as a filler, and the S-Se alloy was applied as a coating. This combination was utilized to create the composite coatings of epoxy/sulfur–selenium (E/S-Se). To investigate the corrosion resistance of this coating on Q235 steel substrate, we conducted measurements and obtained electrochemical impedance spectra (EIS) and linear polarization curves (LPC). These measurements were performed in a three-electrode cell within an electrochemical workstation using a 3.5 wt.% NaCl aqueous solution. By comparing bare Q235 steel, S-Se, and E/S-Se, the study found that the E/S-Se coating had a higher self-corrosion potential (−0.484 V vs. SCE) and the lowest self-corrosion current density ( $2.361 \times 10^{-11}$  A/cm<sup>2</sup>). The purpose was to simulate the corrosive environment experienced by condensate return pipe walls in petroleum refining equipment. Additionally, experiments were carried out using 0.01 mol/L HCl solution as the corrosion medium at different temperatures (40 °C, 60 °C, 80 °C). The results indicated that the E/S-Se coating exhibited a lower corrosion rate compared to the Q235 steel substrate. Under immersion conditions at 40 °C and 60 °C, no corrosive substances were detected on the surface of the coating. The test results demonstrated that the E/S-Se coating exhibited superior corrosion resistance compared to the Q235 substrate, providing up to 99% protection for the substrate.

**Keywords:** Q235 steel; epoxy/S-Se coatings; corrosion performance



**Citation:** Meng, K.; Wei, W.; Wei, K.; Alexandrov, I.V.; An, X.; Wang, D.; Liu, X. Corrosion Performance of Epoxy/Sulfur–Selenium Coating on Q235 Steel. *Coatings* **2024**, *14*, 245. <https://doi.org/10.3390/coatings14030245>

Academic Editor: Alina Vladescu

Received: 18 December 2023

Revised: 15 January 2024

Accepted: 18 January 2024

Published: 20 February 2024



**Copyright:** © 2024 by the authors. Licensee MDPI, Basel, Switzerland. This article is an open access article distributed under the terms and conditions of the Creative Commons Attribution (CC BY) license (<https://creativecommons.org/licenses/by/4.0/>).

## 1. Introduction

Steel is an indispensable metal material in the development of a national economy and plays an important role in our daily life. As an alloy widely used in various industries, Q235 grade steel has a wide range of applications, especially in the fields of defense, infrastructure, ships, and aerospace. However, as Q235 steel is affected by various factors when working in different environments, the corrosion problems it faces cannot be ignored [1]. Especially in the petrochemical industry, with the increasing demand for oil, the quality of the extracted crude oil gradually decreases, and the content of organic chlorine in it increases. In the petroleum refining process, the HCl and H<sub>2</sub>S gases are generated, and liquid water forms a low-temperature corrosive medium HCl–H<sub>2</sub>S–H<sub>2</sub>O. In addition, the petroleum refining equipment at sea has to face the erosion caused by seawater for a long time. Therefore, Q235 steel working in these corrosive media and seawater environment for a long time can easily lead to corrosion and thinning of the pipe wall, and even perforation may occur [2–4]. This causes huge economic losses and serious safety hazards. According

to statistics, on average, about 20% of metal products are degraded and scrapped due to corrosion every year worldwide, resulting in direct economic losses of about USD 2.5 trillion [5].

Over the years, extensive research has been conducted on various strategies to mitigate the corrosion rate of Q235 steel substrate. Commonly employed corrosion prevention methods include surface blue baking, coating, and phosphating technologies [6], as well as the application of corrosion-resistant coatings to the surface of Q235 steel components. The coating applied to the metal substrate needs to possess excellent binding force while also being easy to apply. Acting as a protective barrier, the coating effectively separates the substrate from corrosive substances, thereby enhancing the lifespan of machinery and products. The examples of such coatings include magnetron sputtering ion coatings, polymer coatings, and electrochemical coatings [7].

Zhou et al. [8] have prepared poly-pyrroles films with different doping amounts on the surface of Q235 steel using constant potential electrochemical deposition. The corrosion resistance of poly-pyrrole film on the surface of Q235 steel has been significantly improved compared to bare Q235 steel. Yan et al. [9] have investigated the surface coating of Q235 steel with water-based rust inhibitor and the original Q235 steel corrosion behavior of the original Q235 steel. Compared with the original Q235 steel, the water-based antirust agent-coated Q235 steel has better corrosion resistance under hot and humid environmental conditions and can effectively reduce the corrosion rate. Two-dimensional hexagonal boron nitride materials [10] are reported to have excellent adhesion, barrier, impermeability, and stability and exhibit oxidation resistance to high temperatures (1100 °C) and the corrosive effects of harsh chemicals when used as coatings [11–13]. Govinda et al. [14] have reported that single-layer 2D hexagonal boron nitride coatings are the thinnest insulating coatings with a high inhibition rate of microbial corrosion of 91%. But the fabrication process of hexagonal boron nitride coating is very complicated and expensive, which is not suitable for wide scale application in various industries.

Recent studies have revealed a lightweight sulfur–selenium (S–Se) alloy material with high stiffness and ductility, which has been proven to be an excellent corrosion-resistant coating. In microbial corrosion environments, this alloy demonstrates an impressive 99.9% protection efficiency for steel, along with exceptional barrier properties and high dielectric properties [15,16]. Furthermore, the simple preparation method and significant economic benefits of these coatings contribute to their vast potential for widespread applications. However, there is still a need to improve the bonding between the current S–Se coating and the substrate. In the present, epoxy (ES) was used as a filler, and the S–Se alloy was applied as a coating. This combination was utilized to create the composite coatings of epoxy/S–Se (E/S–Se). The corrosion performance and corrosion resistance mechanism of epoxy/S–Se coating on Q235 steel were investigated.

## 2. Materials and Methods

### 2.1. Feedstock Material

In this paper, the main materials used in the experiment were sulfur powder, selenium powder, Q235, and epoxy. Selenium powder was from Maclean's, and sulfur powder was from China National Pharmaceutical Group. The Q235 steel specimens with dimensions of 15 mm × 15 mm × 3 mm were prepared, whose chemical composition is shown in Table 1 [17]. The objective of the conducted research was to enhance the bonding by incorporating epoxy between the Q235 steel matrix and the S–Se coating. We evaluated the corrosion rate of the S–Se coatings using electrochemical techniques and simulated their corrosion behavior in a petroleum refining environment.

**Table 1.** Chemical composition of Q235 steel (wt. %).

Element	C	Si	Mn	P	S	Cr	Fe
Content%	0.197	0.055	0.233	0.069	0.019	0.105	others

## 2.2. Sample Preparation

Figure 1 shows the binary phase diagram of sulfur–selenium. The crystal structure of the  $\gamma$  phase is monoclinic (Se-type) with the following lattice constants:  $a = 0.11316$  nm,  $b = 0.9104$  nm,  $c = 1.420$  nm, and  $\beta = 142.0^\circ$ . By the solidification of liquid alloys, glassy phases can be prepared often. By heating these glasses, metastable crystalline phases can be obtained [18,19]. Based on the phase diagram, it can be observed that the  $\gamma$  phase is formed at low temperatures when the selenium content ranges from 70 to 88 wt.%. Taking this into consideration, we selected the suitable sulfur-to-selenium mass ratio and conducted further research to achieve improved outcomes.

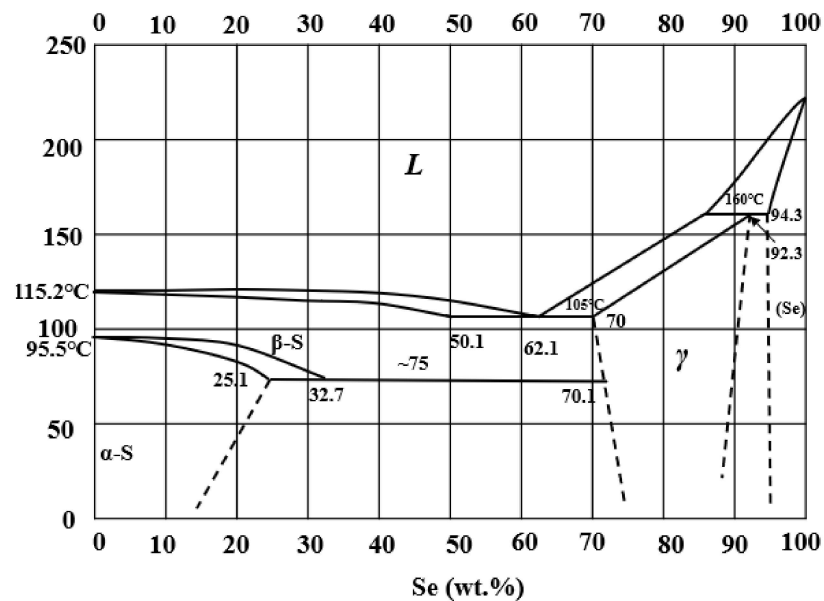


Figure 1. Binary phase diagram of sulfur–selenium.

Sulfur powder and selenium powder were mixed in molar ratio 1:1. The mixture was added to a ball milling tank, and then, zirconia balls with anhydrous ethanol were added, with a mass ratio of sulfur and selenium powders of 1:1.5:1. The rotational speed of the tank was 350 r/min, and it rotated in three dimensions for 1 h. The SEM image of S and Se powders is shown in Figure 2.

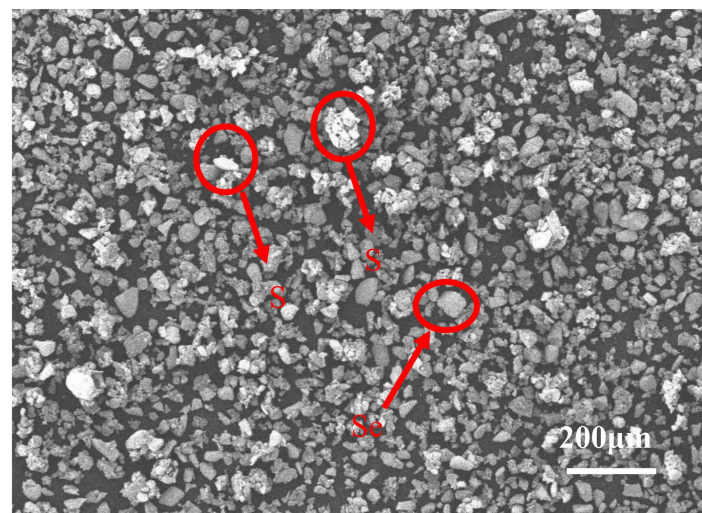
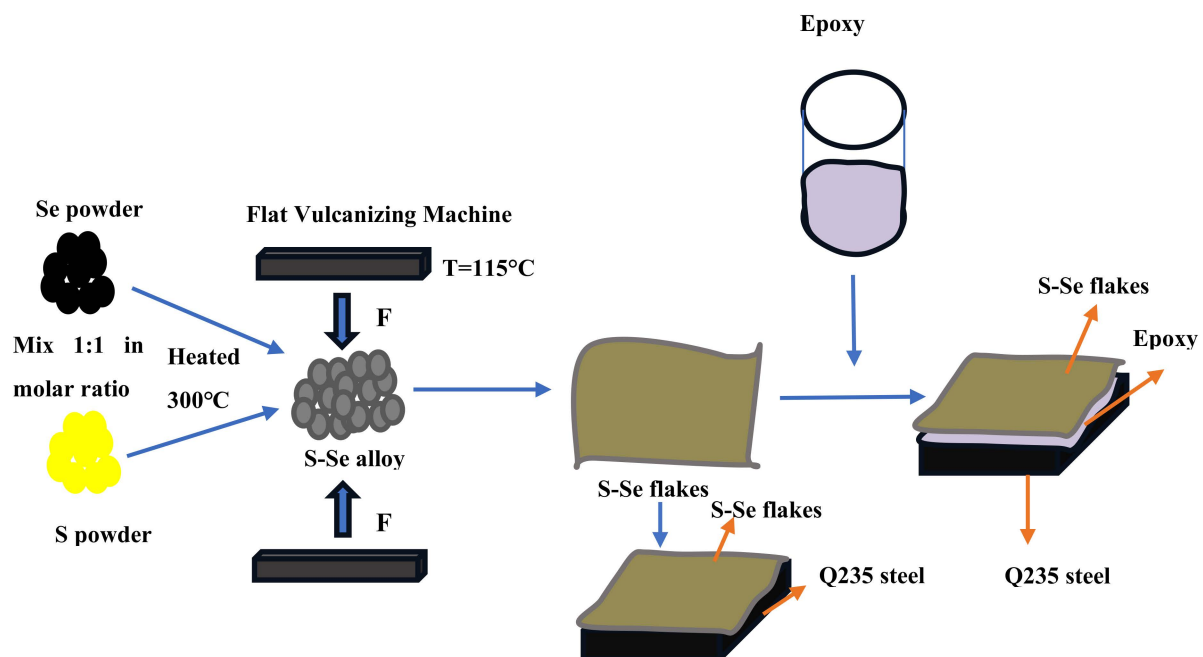


Figure 2. Sulfur powder and selenium powder after ball milling.

Subsequently, the homogeneously mixed powder was placed in an NBD-O1200 tube furnace for sintering. To prevent oxidation, nitrogen gas was continuously supplied throughout the sintering and cooling processes. During the heating process, the temperature was raised to 300 °C and held for 30 min. After the sintering, it was found that the S-Se alloy exhibited an optimal fluidity at 130 °C, allowing for easy and uniform coating onto the Q235 steel substrate. However, the manual coating method failed to ensure the flatness of the coating. In order to address this issue, the following steps were taken. An appropriate amount of sintered S-Se alloy was placed on a plate vulcanizing machine, where it was subjected to a temperature of 115 °C and pressure of 0.25 MPa for 2 min. This treatment resulted in the production of a thin and uniformly thick S-Se sheet, which could then be applied onto the Q235 steel substrate. The samples prepared using this method exhibited uniform thickness and size.

The Q235 steel substrate was ground and polished, and then cleaned with acetone to remove surface oils and impurities. Subsequently, it was rinsed with alcohol and placed in a drying oven at 40 °C for 2 min. The fabrication process of S-Se and E/S-Se coatings is illustrated in Figure 3. The epoxy E44 was thoroughly mixed with the curing agent in a 1:1 ratio until homogeneous. Then, a brush was dipped into the mixture, and a uniform layer was evenly applied onto the Q235 steel substrate. The heating table was set at a temperature of 130 °C, and the epoxy-coated substrate was carefully positioned on it. Next, a precisely cut S-Se sheet was delicately overlaid upon the substrate. Once the S-Se material melted and firmly adhered to the substrate, it was left to naturally cool. This process yielded the desirable E/S-Se coating. The thickness of the epoxy and the S-Se flakes is approximately 28 µm and 276 µm, respectively.



**Figure 3.** Schematic of the coating procedure of S-Se and E/S-Se on Q235 steel.

### 2.3. Electrochemical Measurement

The EIS and kinetic potential LPC of E/S-Se composite coatings were measured using an Auto-lab electrochemical workstation (PGSTAT302N). The corresponding circuit was set up according to the standard three-electrode system. In the experiments, a 3.5 wt.% NaCl solution was chosen as the electrolyte, with the composite coating specimen serving as the working electrode, the Pt mesh as the auxiliary electrode, and the saturated calomel electrode as the reference electrode. Open circuit potentials (OCP) were recorded at the stable stage. The (EIS) were taken at the OCP with an ac sine signal amplitude of 10 mV. The frequency range was from 0.1 Hz to 100 kHz. Potentiodynamic polarization was conducted

in the potential range of plus and minus 0.5 V of the open circuit potentials with the scan rate of 0.1 mV/s.

### 3. Results and Discussion

#### 3.1. Microstructural Analysis

The macroscopic morphology of this coating is displayed in Figure 4a. To examine the morphology of the S-Se alloy, scanning electron microscopy (SEM) was employed, as shown in Figure 4b. Remarkably, the SEM images revealed the absence of any pores within the S-Se coating, revealing its orderly and stratified structure. The surface is a slightly raised crease. Furthermore, the surface roughness of the S-Se coating, measured with a laser confocal microscope, is depicted in Figure 4c. Notably, the surface appeared remarkably smooth and level without any noticeable irregularities. The recorded surface roughness value was found to be 21.76  $\mu\text{m}$ . Figure 4d illustrates two distinctive Raman peaks at 255  $\text{cm}^{-1}$  and 351  $\text{cm}^{-1}$ , respectively. These peaks serve as characteristic signatures of the S-Se alloy, confirming the presence of S-Se components within the coating.

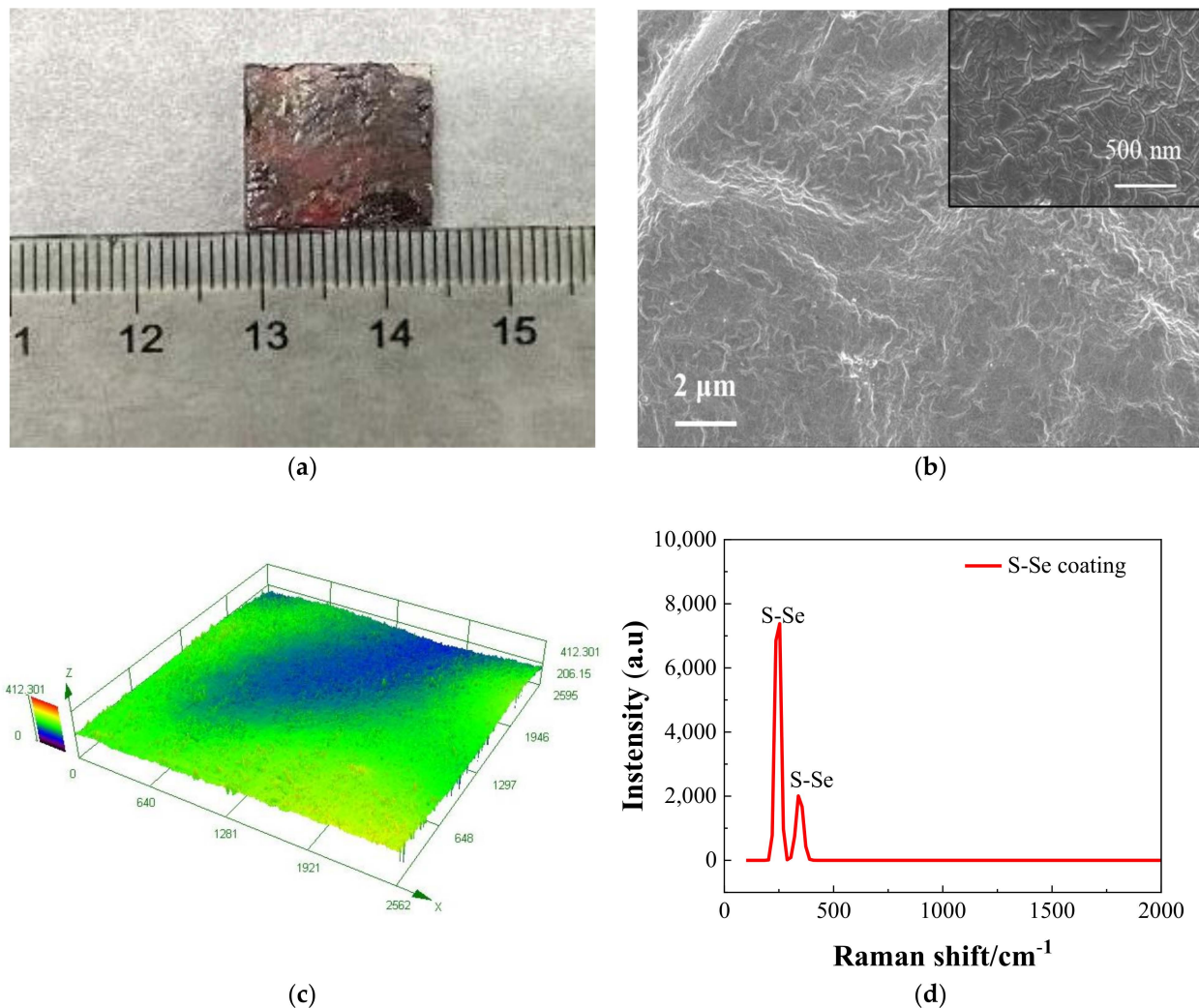


**Figure 4.** S-Se coating: (a) macro topography image, (b) SEM image, (c) surface roughness, and (d) Raman spectroscopy pattern.

### 3.2. Binding Force

The different coefficients of thermal expansion between the coating and the base material generate thermal stresses during cooling, severely impacting the bonding strength at the interface [20,21]. The significant difference in thermal expansion coefficients between S-Se alloy and Q235 steel particularly affects interfacial bonding, as shown in Figure 5. In Figure 5a, visible gaps indicate poor bonding between the S-Se coating and Q235 steel. Introducing an adhesion promoter, epoxy, enhances the affinity between the coating and the substrate and improves their bonding, as demonstrated in Figure 5b. S-Se coating thickness of approximately 276  $\mu\text{m}$ , epoxy resin thickness of approximately 28  $\mu\text{m}$ . This improvement significantly extends the coating's service life, enhancing durability and overall performance and resulting in a superior and long-lasting product.

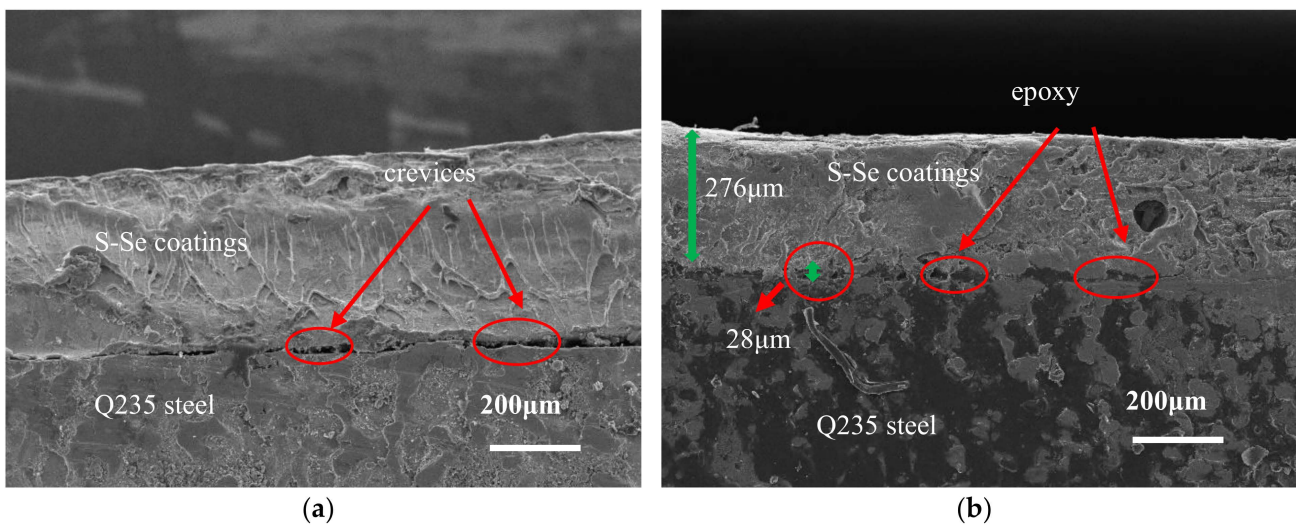


**Figure 5.** Lateral morphology of coatings and substrates: (a) S-Se coatings and (b) E/S-Se coatings.

The cross-hatching grid method was chosen for this experiment to assess the bonding strength of the coating. Firstly, vertical cross-hatching was performed on the coating surface using a precision blade, followed by the careful application of a 25 mm wide tape over the hatched grid, which was subsequently peeled off at a specific angle. The test results were evaluated in accordance with the GB/T9286-1998 standard [22], which outlines the scribing experiment for color paint and varnish film. Figure 6a,b reveal the macroscopic morphology of the S-Se coating and the E/S-Se coating bonding experiment. It is evident that the S-Se coating has completely detached, with the detached area exceeding 65% of the tested coating surface, indicating a bonding rating of five. Conversely, the E/S-Se coating exhibited only a minimal detachment at the intersection of the cuts, with the detached area being less than 15% of the tested coating surface but more than 5%, resulting in an adhesion rating of two. Figure 6c,d provide the microscopic images of the cross-hatched E/S-Se and S-Se coatings, further substantiating the enhanced bonding between the coating and the substrate due to the presence of epoxy. Notably, Figure 6e,f demonstrate that the E/S-Se coating possesses a smoother and more uniform surface compared to the S-Se coating, which exhibits significant areas of exfoliation leading to an uneven surface profile with roughness measurements of 26.2  $\mu\text{m}$  and 81.4  $\mu\text{m}$ , respectively.

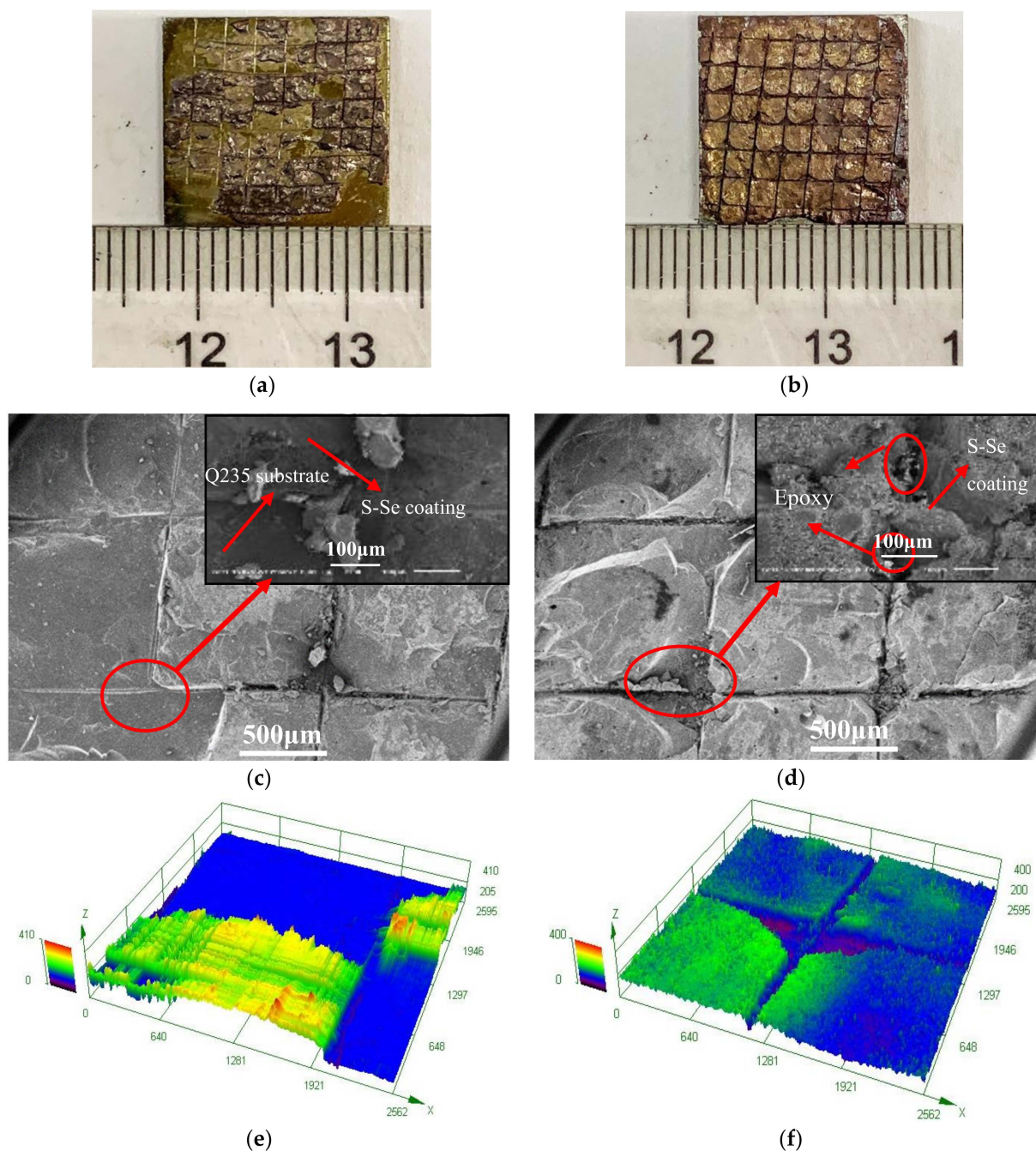


**Figure 6.** S-Se and E/S-Se coatings' cross-hatch topography: macro topography of (a) S-Se coating and (b) E/S-Se coating, SEM of (c) S-Se coating and (d) E/S-Se coating, and surface roughness of (e) S-Se coating and (f) E/S-Se coating.

### 3.3. Electrochemical Testing

To further study the corrosion mechanism of the coating and the specimen, the Nyquist plot and the Bode plot of the E/S-Se coating, S-Se coatings, and Q235 steel were drawn (Figure 7). The radius in the Nyquist diagram is the capacitive reactance. They have similar impedance characteristics. This is typical of pitting corrosion. As corrosion begins, the activation zone becomes smaller and smaller, and the capacitive reactance ring gradually expands. It is generally accepted that the larger the radius of the capacitive reactance arc, the higher the impedance and the lower the electrode activity. It is generally believed that this is due to the unstable condition on the surface due to the emergence of pitting corrosion [23–25].

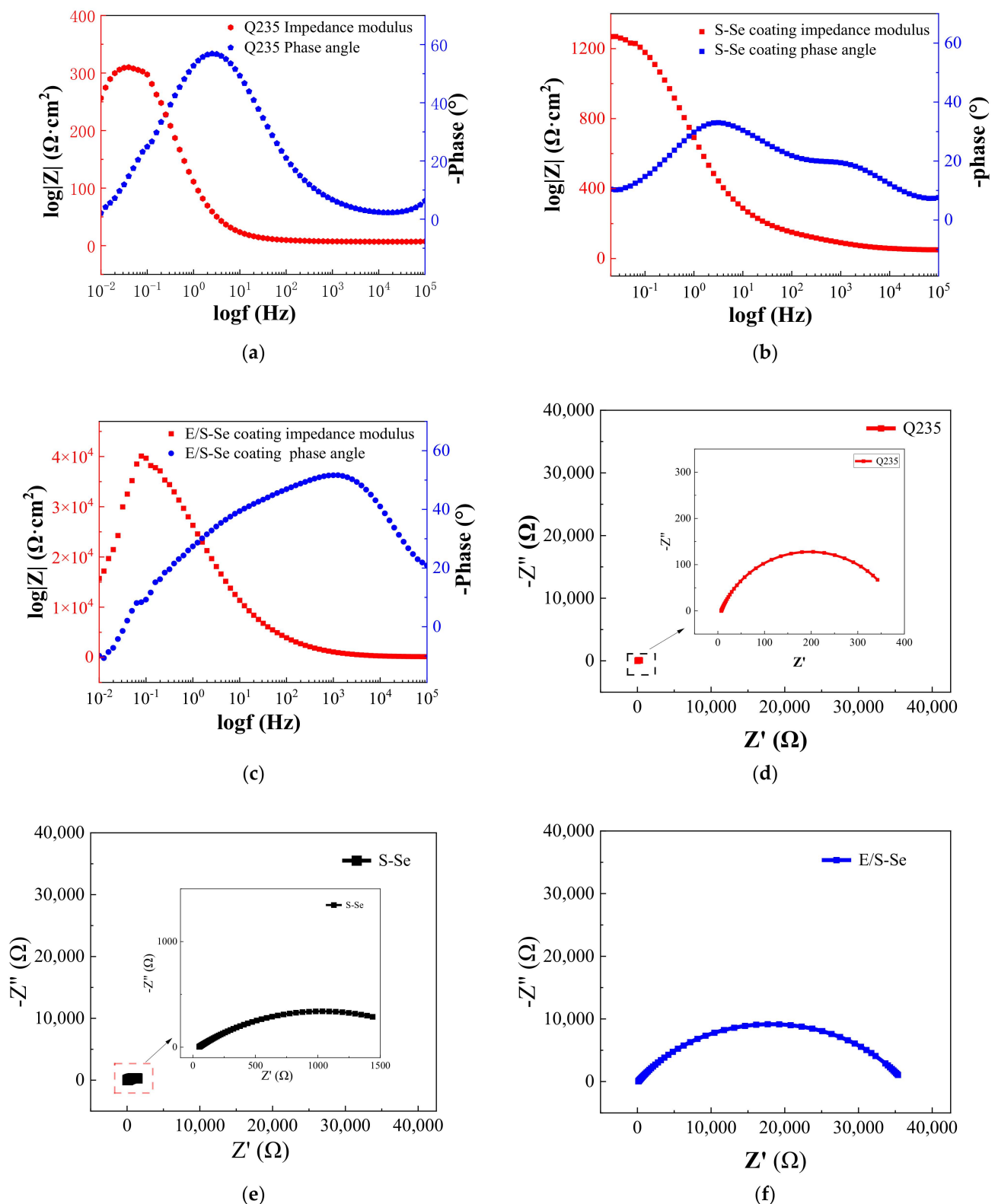


**Figure 7.** The EIS of E/S-Se coating and Q235 steel: (a) Bode plot of Q235 steel, (b) Bode plot of S-Se coating, (c) Bode plot of E/S-Se coating, (d) Nyquist plot of Q235 steel, (e) Nyquist plot of S-Se coating, and (f) Nyquist plot of E/S-Se coating.

Figure 7a–c depict the Bode plot, where the impedance modulus and the phase angle peak in the low- and mid-frequency regions often serve as the indicators of the coating’s

corrosion resistance quality. The impedance modulus and the phase angle peak initially increase and then decrease. Notably, the E/S-Se coating exhibits the highest impedance modulus, while the phase angle peak remains relatively consistent. This indicates the excellent corrosion resistance of the coating. Moreover, the radius of the capacitive arc resistance is an important parameter for evaluating the corrosion resistance of materials, as a larger radius corresponds to a stronger corrosion resistance [26]. As illustrated in Figure 7d–f, the E/S-Se coating, the S-Se coating, and the Q235 steel substrate show an increasing and then a decreasing trend for the radius of the capacitive arc resistance. However, the E/S-Se coating demonstrates a significantly larger radius compared to the S-Se coating and the Q235 steel substrate, signifying a superior corrosion resistance.

The E/S-Se coatings were immersed in a 3.5 wt.% NaCl solution, and the OCP change curves of the coatings were observed over time. In general, the open-circuit potential of a material reflects its susceptibility to electrochemical corrosion [26]. A higher open-circuit potential indicates a lower tendency for corrosion to occur. Upon examining Figure 8a, it is evident that the OCP of the E/S-Se coating exhibits significant fluctuations. This can be attributed to the unevenness of the coating surface and the presence of microscopic defects such as oxides. However, it is noteworthy that the E/S-Se coating demonstrates a higher open-circuit potential compared to those of the S-Se coating and the Q235 steel, which suggests a reduced susceptibility to corrosion.

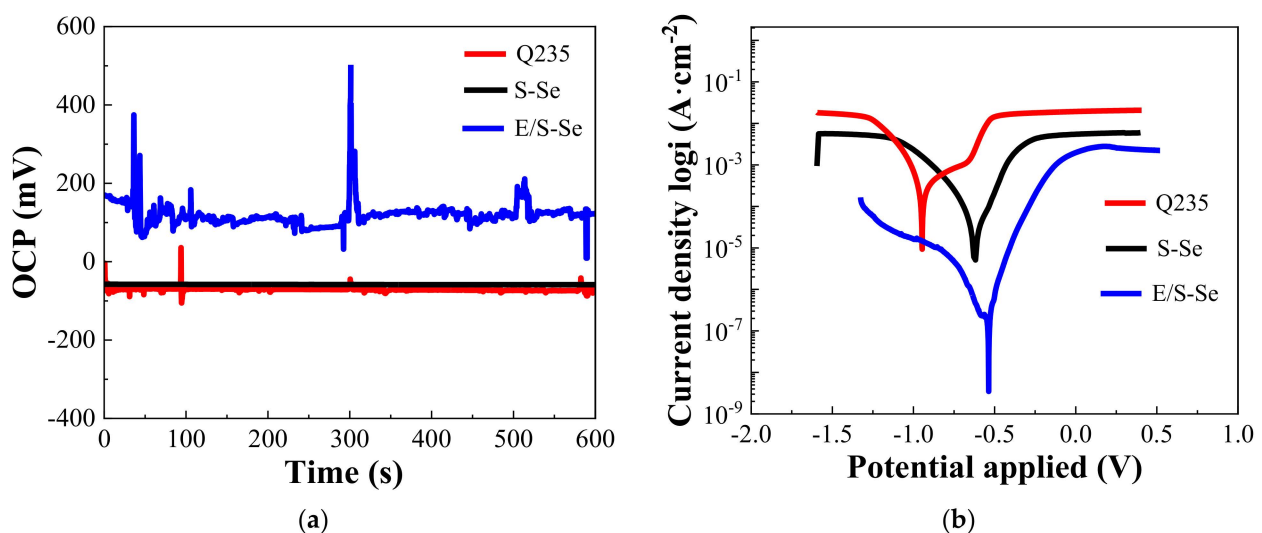


**Figure 8.** (a) Open circuit potential plot and (b) LPC plot.

Figure 8b shows the LPC curves. The E/S-Se coating has a higher applied potential compared to those of the S-Se coating and the bare Q235 steel. It is evident that the E/S-Se coating has a better corrosion resistance. The electrochemical parameters such as corrosion current density ( $I_{\text{corr}}$ ), corrosion rate, and corrosion potential ( $E_{\text{corr}}$ ) are presented in Table 2. It was calculated by the extrapolation of linear segments of anodic and cathodic Tafel slopes [9,27]. As can be seen from Table 2, the E/S-Se coating has the highest self-corrosion potential ( $-0.484$  V) and the lowest self-corrosion current density ( $2.361 \times 10^{-11}$  A/cm<sup>2</sup>). It has the highest polarization resistance value,  $R_p$ , of  $4.904 \times 10^8$   $\Omega \cdot \text{cm}^2$ .

**Table 2.** Potentiodynamic polarization parameters of Q235 steel and E/S-Se coating in 3.5 wt.% NaCl solution.

Item	$E_{\text{corr}}$ (V vs. SCE)	$I_{\text{corr}}$ (A)	$j_{\text{corr}}$ (A/cm <sup>2</sup> )	Polarization Resistance ( $\Omega$ )
Q235	$-0.979$	$2.449 \times 10^{-4}$	$1.088 \times 10^{-4}$	106.41
S-Se	$-0.622$	$2.910 \times 10^{-5}$	$1.293 \times 10^{-5}$	89,547
E/S-Se	$-0.484$	$5.313 \times 10^{-11}$	$2.361 \times 10^{-11}$	$4.904 \times 10^8$

### 3.4. Electrochemical Corrosion Mechanism

According to the literature, it is anticipated that redox reactions will occur in Q235 steel immersed in a sodium chloride solution without a protective film [28,29]. The potential difference between the metals leads to the galvanic coupling corrosion of the substrate, which puts the use of less active metals protected by coatings on hold [30,31]. The specific reactions are as follows:



Based on the above ionic reactions, it can be observed that in air-saturated sodium chloride solution, Q235 steel undergoes electrochemical reactions to produce  $\text{Fe}^{2+}$ , which then reacts with  $\text{OH}^{-}$  from electrolysis to create iron oxides. This generates yellowish-brown corrosion products that deposit onto the steel surface. In contrast, Q235 steel with an E/S-Se coating has reduced ion exchange due to the coating's superior barrier and high dielectric properties (as shown in Figures 7 and 8), indicating excellent corrosion resistance. The corrosion mechanism is illustrated in Figure 9.

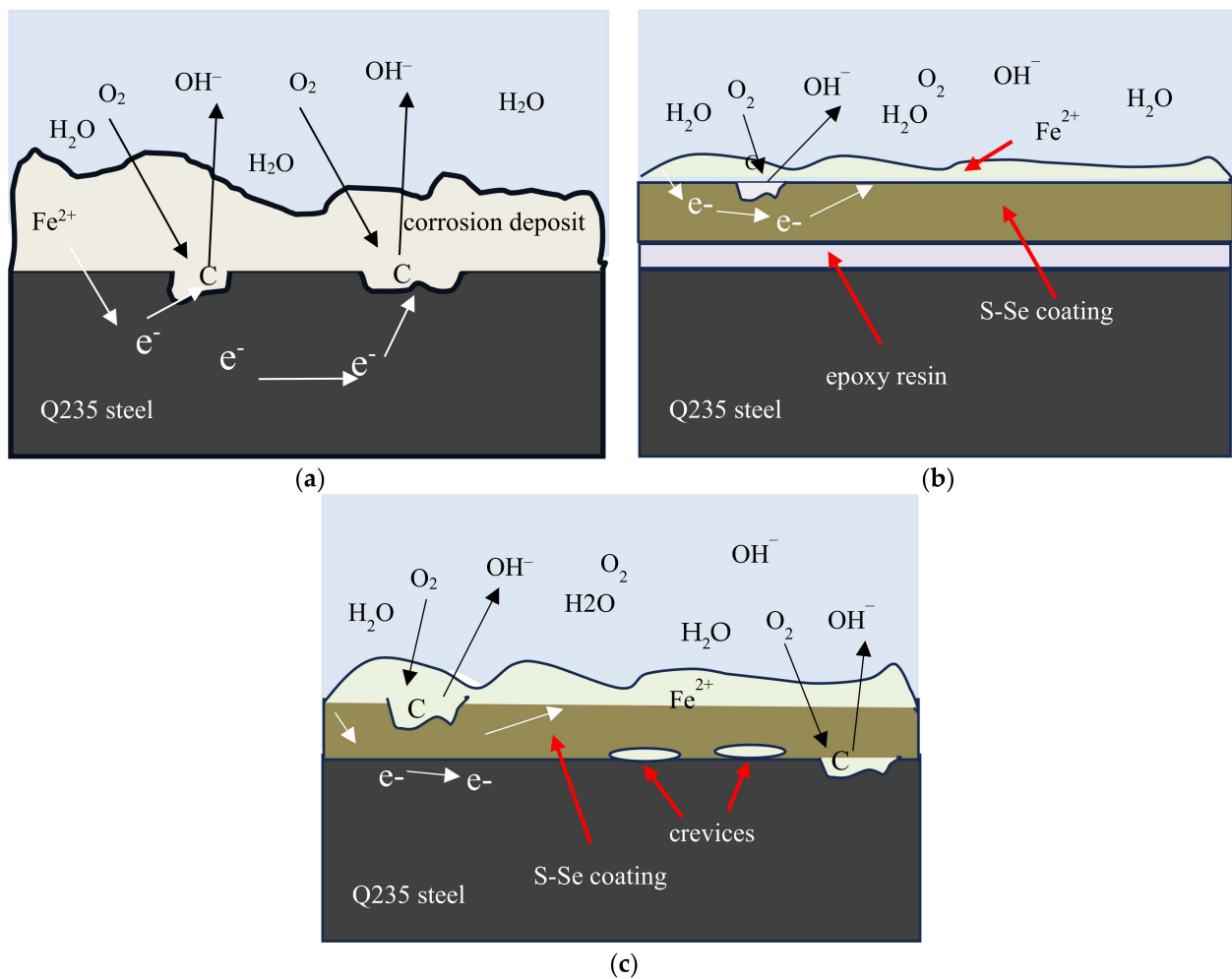


**Figure 9.** Schematic diagram of corrosion mechanism: (a) Q235 steel, (b) S-Se coating, and (c) E/S-Se coating.

### 3.5. Corrosion Weightlessness Experiment

Figure 10 illustrates the changes in mass loss and surface morphology of the E/S-Se coating. The Q235 steel substrate is immersed for 120 h in a simulated environment resembling the reflux condensation tubes at the top of a petroleum refinery atmospheric tower. The corrosive medium used in the experiments was a 0.01 mol/L HCl solution, and the temperature ranged from 37.2 °C to 69 °C [32,33]. Both the E/S-Se coating and the Q235 steel substrate were subjected to immersion in the same concentration of corrosive medium at temperatures of 40 °C, 60 °C, and 80 °C.

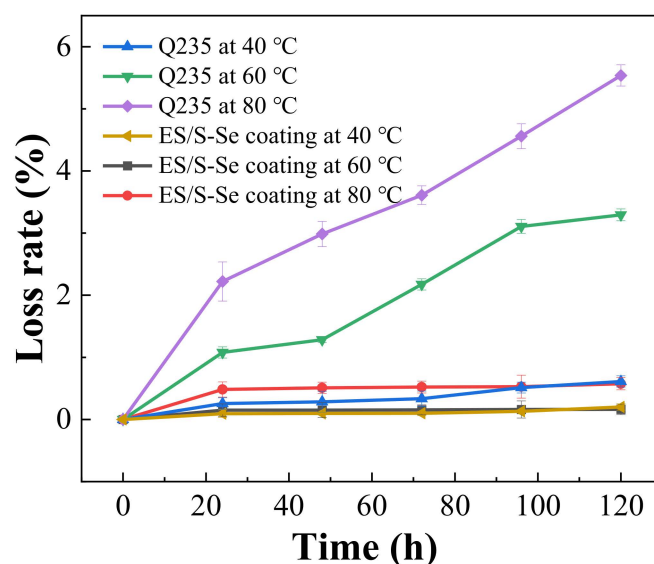
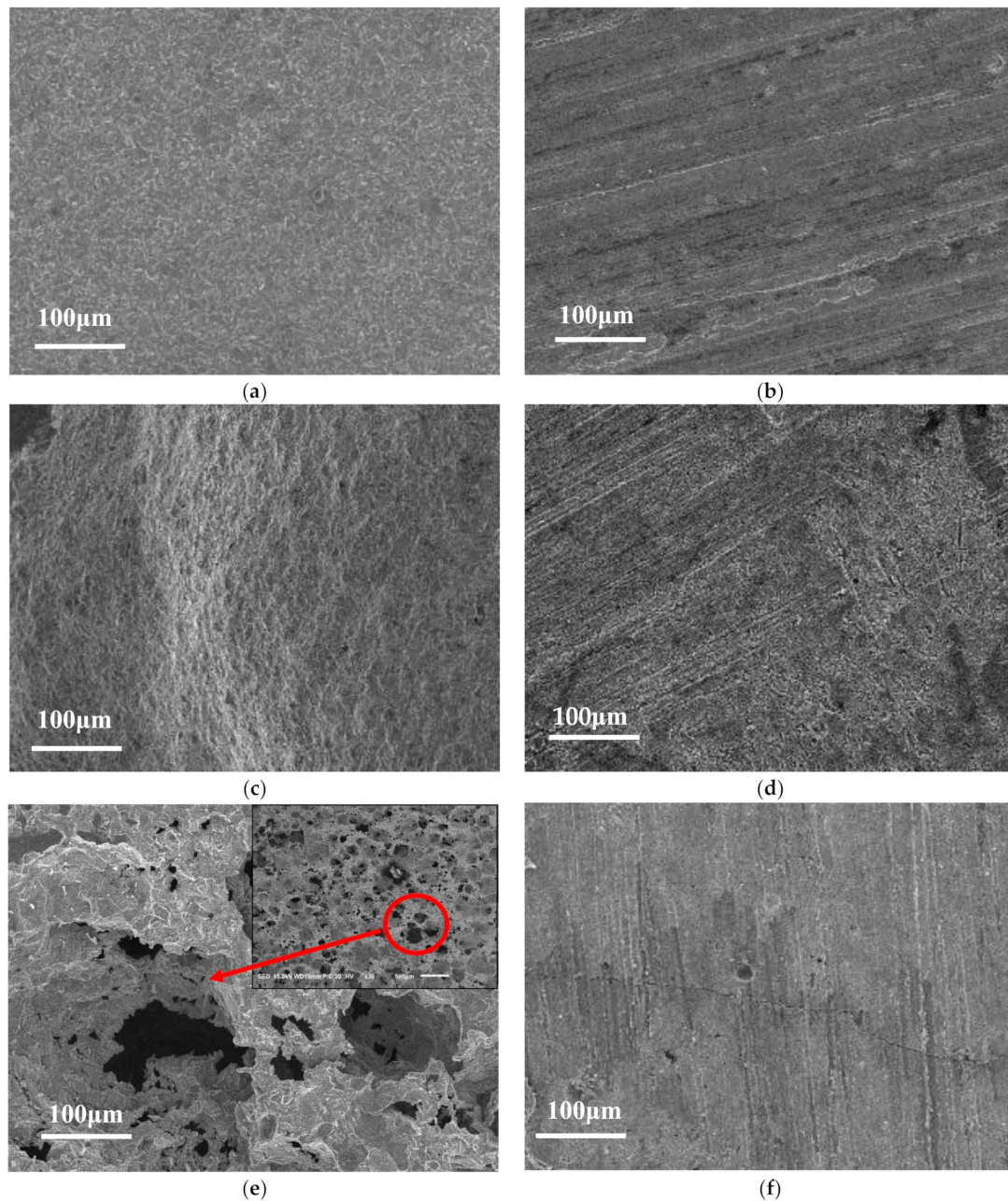


Figure 10. Corrosion weight loss at different temperatures (immersion in 0.1 mol/L HCl for 120 h).

From Figure 10, it is evident that both the coating and the substrate experienced mass loss during the immersion process. This can be attributed to ion exchange between the corrosion medium and the E/S-Se coating, as well as the Q235 steel substrate, leading to electrochemical reactions and the formation of easily detachable oxides on the surface. As the temperature increased, the intensity of electron exchange escalated, resulting in a corresponding upward trend in corrosion weight loss. Importantly, the E/S-Se coating exhibited a significantly lower corrosion weight loss rate compared to that of the Q235 steel substrate.

Being immersed at 40 °C (Figure 11a), the Q235 steel matrix surface had a small amount of oxide shedding. At 60 °C (Figure 11c), the Q235 steel substrate displayed a furrowed laminar morphology, while at 80 °C (Figure 11d), copious porous corrosion products were generated on its surface, ultimately resulting in cavities forming in the initial layer. A prolonged exposure to this environment rendered the Q235 steel substrate susceptible to corrosion perforation issues. Concurrently, at 40 °C and 60 °C (Figure 11b,d), the E/S-Se coatings' surface underwent minimal changes. However, at 80 °C (Figure 11f), fine cracks emerged due to prolonged exposure to relatively high temperatures, thereby causing agglomeration and cracking within the coatings. Nevertheless, the integrity of the reflux condenser tube atop the petroleum refining atmospheric pressure tower was effectively preserved with the aid of the E/S-Se coating. Thanks to its protective properties, the corrosion rate was significantly minimized, successfully achieving the desired goal of safeguarding the condenser tube.



**Figure 11.** Corrosion weight loss at different temperatures (immersed in 0.1 mol/L HCl for 120 h): (a,c,e) Q235 steel immersed at 40, 60, and 80 °C, respectively, and (b,d,f) E/S-Se coating immersed at 40, 60 and 80 °C, respectively.

#### 4. Conclusions

The coating on Q235 steel was prepared using epoxy, sulfur powder, and selenium powder as raw materials. Q235 steel and S-Se coatings were used as the control group for corrosion inhibition tests. The results obtained from EIS and dynamic potential polarization experiments demonstrated that the presence of the E/S-Se coating limited the charge transfer at the electrolyte interface and effectively protected Q235 steel in a 3.5 wt.% NaCl solution from electrolyte penetration. Immersion trials revealed that the surface of Q235 steel exhibited numerous corrosive etching holes, whereas the surface of the E/S-Se coating showed no significant changes, and only minimal corrosion products were observed. This indicates that the E/S-Se coating effectively prevents the corrosion of Q235 steel. In summary, the E/S-Se coating provides effective protection to Q235 steel against corrosive

substances during the operation of the reflux condenser tube in the atmospheric pressure tower. Additionally, the epoxy coating exhibits stronger bonding strength than the pure S-Se coating, with an adhesion force reaching level 2.

**Author Contributions:** Conceptualization, W.W.; Methodology, K.W. and I.V.A.; Validation, K.W. and X.A.; Formal analysis, K.W. and D.W.; Investigation, K.M.; Data curation, X.A. and X.L.; Writing—original draft, K.M.; Writing—review & editing, W.W. and I.V.A.; Visualization, D.W. and X.L.; Supervision, W.W. All authors have read and agreed to the published version of the manuscript.

**Funding:** This research was funded by Jiangsu Carbon Peak Carbon Neutrality Science and Technology Innovation Project (BE2022044), Jiangsu International Science and Technology Project (BZ2021078), International Chinese Education Innovation Project of Ministry of Education of China (21YH011CX5), and Changzhou Science and Technology Project (CZ20210003).

**Institutional Review Board Statement:** Not applicable.

**Informed Consent Statement:** Not applicable.

**Data Availability Statement:** All the data used to support the findings of this study are present in the paper.

**Conflicts of Interest:** The authors declare no conflicts of interest.

## References

1. Wang, C.; Han, J.; Zhang, C.; Su, Y.; Zhang, S.; Zhang, Z.; Wang, T. Temperature dependence of interface characterization and mechanical properties of TA1/Q235 composite fabricated by explosive welding. *Adv. Eng. Mater.* **2023**, *25*, 2201759. [[CrossRef](#)]
2. Ou, G.; Wang, K.; Sun, Y.; Sun, L. Analysis of flow corrosion failure of atmospheric distillation tower overhead heat exchanger system and prediction study. *Corros. Prot. Petrochem.* **2015**, *32*, 1–5.
3. Zhang, Z.; Zhang, Y.; Chen, W. Cause analysis and countermeasures for corrosion perforation of atmospheric tower wall. *Safety Health Environ.* **2020**, *20*, 15–19.
4. Tu, L. Corrosion analysis and countermeasures of atmospheric tower top tray. *Corros. Prot. Petrochem.* **2020**, *37*, 58–61.
5. Shi, L.J. Research on Corrosion Behavior of Three Metals in Marine Environment and Finite Element Simulation. Ph.D. Thesis, University of Science and Technology of China, Hefei, China, 2021.
6. Zhang, X.-F.; Jiang, F.; Chen, R.-J.; Chen, Y.-Q.; Hu, J.-M. Robust superhydrophobic coatings prepared by cathodic electrophoresis of hydrophobic silica nanoparticles with the cationic resin as the adhesive for corrosion protection. *Corros. Sci.* **2020**, *173*, 108797. [[CrossRef](#)]
7. Yu, Z.; Zhou, C.; Liu, R.; Zhang, Q.; Gong, J.; Tao, D.; Ji, Z. Fabrication of superhydrophobic surface with enhanced corrosion resistance on H62 brass substrate. *Colloids Surf. A* **2020**, *589*, 124475. [[CrossRef](#)]
8. Zhou, W.; Wu, K.; Zhang, K.; Wang, Z.; Liu, Z.; Hu, S.; Fang, Y.; He, C. Studies on corrosion behaviors of q235 steel coated by the polypyrrole films doped with different dopants. *Int. J. Electrochem. Sci.* **2020**, *15*, 2594–2603. [[CrossRef](#)]
9. Yan, Z.; Kang, M.; Tan, Z.; Li, Q.; Tian, B.; Li, S. Prevention of Q235 steel corrosion using waterborne rust inhibitor. *J. Wuhan Univ. Technol. Sci. Ed.* **2023**, *38*, 206–211. [[CrossRef](#)]
10. Rajiv, S.; Shanmugam, K. Robust superhydrophobic composite coating using h-BN/MWCNT via supercritical fluid processing. *J. Coat. Technol. Res.* **2023**, *20*, 2135–2141. [[CrossRef](#)]
11. Liu, Z.; Gong, Y.; Zhou, W.; Ma, L.; Yu, J.; Idrobo, J.C.; Jung, J.; MacDonald, A.H.; Vajtai, R.; Lou, J.; et al. Ultrathin high-temperature oxidation-resistant coatings of hexagonal boron nitride. *Nat. Commun.* **2013**, *4*, 2541. [[CrossRef](#)]
12. Zhang, J.; Yang, Y.; Lou, J. Investigation of hexagonal boron nitride as an atomically thin corrosion passivation coating in aqueous solution. *Nanotechnology* **2016**, *27*, 364004. [[CrossRef](#)] [[PubMed](#)]
13. Husain, E.; Narayanan, T.N.; Taha-Tijerina, J.J.; Vinod, S.; Vajtai, R.; Ajayan, P.M. Marine corrosion protective coatings of hexagonal boron nitride thin films on stainless steel. *ACS Appl. Mater. Interfaces* **2013**, *5*, 4129–4135. [[CrossRef](#)] [[PubMed](#)]
14. Chilkoor, G.; Karanam, S.P.; Star, S.; Shrestha, N.; Sani, R.K.; Upadhyayula, V.K.K.; Ghoshal, D.; Koratkar, N.A.; Meyyappan, M.; Gadhamshetty, V. Hexagonal boron nitride: The thinnest insulating barrier to microbial corrosion. *ACS Nano* **2018**, *12*, 2242–2252. [[CrossRef](#)] [[PubMed](#)]
15. Susarla, S.; Chilkoor, G.; Kalimuthu, J.R.; Saadi, M.A.S.R.; Cui, Y.; Arif, T.; Tsafack, T.; Puthirath, A.B.; Sigdel, P.; Jasthi, B.; et al. Corrosion resistance of sulfur-selenium alloy coatings. *Adv. Mater.* **2021**, *33*, 2104467. [[CrossRef](#)] [[PubMed](#)]
16. Susarla, S.; Tsafack, T.; Owuor, P.S.; Puthirath, A.B.; Hachtel, J.A.; Babu, G.; Apte, A.; Jawdat, B.L.; Hilario, M.S.; Lerma, A.; et al. High-K dielectric sulfur-selenium alloys. *Sci. Adv.* **2019**, *5*, eaau9785. [[CrossRef](#)] [[PubMed](#)]
17. Bian-Li, Q.; Jun-Qi, L.; Chao-Yi, C. Synergy corrosion effect of thiosulfate and sulfide on Q235 steel in sodium aluminate solution. *Mater. Res. Express* **2018**, *6*, 025607. [[CrossRef](#)]
18. Weiss, J. Mitteilung über Interchalkogenverbindungen. IV. Röntgenographische Untersuchungen an Mischkristallen der Zusammensetzung  $Se_nS_{8-n}$ . *Z. Anorg. Allg. Chem.* **1977**, *435*, 113–118. [[CrossRef](#)]

19. Maekawa, T.; Yokokawa, T.; Niwa, K. The Enthalpies of binary mixtures of chalcogen elements. *Bull. Chem. Soc. Jpn.* **1973**, *46*, 761–765. [[CrossRef](#)]
20. Zhang, Y.K.; Kong, D.J.; Feng, A.X.; Lu, J.Z.; Zhang, L.H.; Ge, T. Study on the determination of interfacial binding strength of coatings (I): Theoretical analysis of stress in thin film binding interface. *Acta Phys. Sin.* **2006**, *6*, 2897–2900. [[CrossRef](#)]
21. Ghazali, N.; Basirun, W.J.; Nor, A.M.; Johan, M.R.; Rahman, F.A. Corrosion-resistant super-amphiphobic (PVDF-fnAl<sub>2</sub>O<sub>3</sub>) coating with thermal and mechanical stability. *J. Coat. Technol. Res.* **2023**, *23*, 1–11. [[CrossRef](#)]
22. GB/T9286-1998; Paints and Varnishes—Cross Cut Test for Films. Standardization Administration of China: Beijing, China, 1998.
23. Belghiti, M.; Echihi, S.; Mahsoune, A.; Karzazi, Y.; Aboulmouhajir, A.; Dafali, A.; Bahadur, I. Piperine derivatives as green corrosion inhibitors on iron surface; DFT, Monte Carlo dynamics study and complexation modes. *J. Mol. Liq.* **2018**, *261*, 62–75. [[CrossRef](#)]
24. Li, X.-H.; Deng, S.-D.; Fu, H. Adsorption and inhibitive action of hexadecylpyridinium bromide on steel in phosphoric acid produced by dihydrate wet method process. *J. Appl. Electrochem.* **2011**, *41*, 507–517. [[CrossRef](#)]
25. Rbaa, M.; Benhiba, F.; Abousalem, A.S.; Galai, M.; Rouifi, Z.; Oudda, H.; Lakhri, B.; Warad, I.; Zarrouk, A. Sample synthesis, characterization, experimental and theoretical study of the inhibitory power of new 8-hydroxyquinoline derivatives for mild steel in 1.0 M HCl. *J. Mol. Struct.* **2020**, *1213*, 128155. [[CrossRef](#)]
26. Cao, C.; Zhang, J. *An Introduction Electrochemical Impedance Spectroscopy*; China Science Publishing: Beijing, China, 2002.
27. Jessima, S.H.M.; Subhashini, S.; Berisha, A.; Oral, A.; Srikandan, S.S. Corrosion mitigation performance of disodium EDTA functionalized chitosan biomacromolecule—Experimental and theoretical approach. *Int. J. Biol. Macromol.* **2021**, *178*, 477–491. [[CrossRef](#)] [[PubMed](#)]
28. Chen, S.; Zhang, D. Corrosion behavior of Q235 carbon steel in air-saturated seawater containing *Thalassospira* sp. *Corros. Sci.* **2019**, *148*, 71–82. [[CrossRef](#)]
29. Zhang, B.; Zhang, Z.; Dong, Q.; Wu, J.-S.; Zhuang, N.; Zuo, P.; Li, X. Electrochemical corrosion behavior of nanostructured BCC Al<sub>0.5</sub>CoCrFeNi<sub>0.4</sub> high entropy alloy in sodium chloride solution. *Trans. Nonferrous Met. Soc. China* **2023**, 1–22.
30. Hwang, S.-H.; Lee, S.-H.; Lee, M.-H. Influence of heat treatment on corrosion resistance of Sn/Mg films formed by PVD method on hot-dip galvanized steel. *Coatings* **2023**, *13*, 196. [[CrossRef](#)]
31. Penyashki, T.; Kostadinov, G.; Kandeveva, M.; Kamburov, V.; Nikolov, A.; Dimitrova, R. Abrasive and erosive wear of Ti6Al4V alloy with electrospark deposited coatings of multicomponent hard alloys materials based of WC and TiB<sub>2</sub>. *Coatings* **2023**, *13*, 215. [[CrossRef](#)]
32. Chen, B.C.; Zhang, L.; Han, L.; Zhang, Y.; Qu, D.; Liu, X. Study on dew point corrosion with multiphase flow simulation at the overhead vapor line of the atmospheric tower. *Saf. Health Environ.* **2018**, *18*, 49–54.
33. Wang, Y.; Yang, L.; Zhang, Y. Analysis of scale formation in the overhead volatile line and the corrosion inhibitor pipeline of a crude oil unit. *Chem. Eng.* **2015**, *29*, 51–54.

**Disclaimer/Publisher’s Note:** The statements, opinions and data contained in all publications are solely those of the individual author(s) and contributor(s) and not of MDPI and/or the editor(s). MDPI and/or the editor(s) disclaim responsibility for any injury to people or property resulting from any ideas, methods, instructions or products referred to in the content.